Development of attapulgite/$Ce_{1-x}Zr_xO_2$ nanocomposite as catalyst for the degradation of methylene blue

Xiazhang Li [a,b], Chaoying Ni [c,*], Chao Yao [a], Zhigang Chen [d]

[a] School of Petrochemical Engineering, Changzhou University, Changzhou 213164, PR China
[b] Jiangsu Key Laboratory for Solar Cell Materials and Technology, Changzhou University, Changzhou 213164, PR China
[c] Department of Materials Science and Engineering, University of Delaware, Newark, DE 19716, USA
[d] Jiangsu Key Laboratory for Environment Functional Materials, Suzhou University of Science and Technology, Suzhou 215009, PR China

ARTICLE INFO

ABSTRACT

Novel attapulgite (ATP)/$Ce_{1-x}Zr_xO_2$ nanocomposite was prepared by a facile homogeneous deposition method using hexamethylenetetramine as precipitator. The catalytic activity of ATP/$Ce_{1-x}Zr_xO_2$ was investigated by oxygenating methylene blue dye wastewater using O_3 as oxidant. HRTEM, XRD, FT-IR, Raman and H_2-TPR data reveal significant interactions between Ce—Zr—O oxides and ATP support, the evolution of textural, structural and oxidation state as a function of the composition, and the formation of more oxygen vacancies in $Ce_{1-x}Zr_xO_2$. The molar fraction of Zr^{4+} demonstrates considerable influence on the degradation rate of the methylene blue. Compared with pure ATP and ATP/CeO_2, the ATP/$Ce_{1-x}Zr_xO_2$ composite remarkably enhances catalytic activity, and a maximum degradation rate of methylene blue at 99% is achieved when the molar fraction x is 0.2.

1. Introduction

Catalytic wet oxidation is an abatement method which uses dissolved oxidants to catalytically destroy target organic pollutants in wastewater streams. The use of solid catalysts has attracted considerable attention because they not only allow oxidative treatment under moderate severity, but also offer a versatile process wherein the catalyst can be conveniently recovered and reused [1]. Since the nature of the support is of critical importance to the catalytic performance of the resultant catalysts, a variety of supports, including metal oxides [2,3], zeolites [4–6], mesoporous silicas [7–9], carbon based structures (carbon nanotube, graphene, mesoporous carbon, etc.) [10–12], mineral materials [13–15], have been used for preparing the solid composite catalysts. However, the exploration of new catalyst systems with better performance, easier availability and fabrication, and reduced cost remains to be a challenge.

Attapulgite (ATP) is a natural hydrated magnesium aluminum silicate having 1-D fibrous morphology with a diameter in nanometers and a length from several hundreds of nanometers to a few micrometers [16,17]. It has large surface area exhibiting excellent activity and chemical adsorption property. Liu et al. [18] prepared ATP/Fe_3O_4 composites by a co-precipitation technique and found that the composite showed enhanced magnetic properties.

Cao et al. [19] synthesized ATP/CuO composites by a deposition-precipitation method demonstrating good activity for CO oxidation at low temperatures. Zhao et al. [20,21] prepared silver and copper modified ATP/TiO_2 photocatalysts by a hydrolysis method for the degradation of methylene blue. Huo et al. [22] developed the synthesis of ATP/ZnO composites for antibacterial activity against *E. coli*. Zhang et al. [23] obtained ATP/SnO_2–TiO_2 via an in situ sol–gel method and investigated its photocatalytic removal ability of the methyl orange under ultraviolet radiation.

With respect to the degradation of pollutants, one of the main problems with catalytic oxidation of organic compounds is the general deficient proportion of hydroxyl radical (OH•) during the reaction [24,25]. In order to increase the OH• supply from the oxidant, materials with oxygen storage capacity such as CeO_2 are of significant interest. Several efforts have been made to fabricate CeO_2 based materials as heterogeneous catalyst for waste water treatment [26–29]. However, to the best of authors' knowledge, report on the ATP/CeO_2 composite is very rare. It is worth mentioning that in our previous work, we successfully prepared well-defined CeO_2 nanotubes templated by modified-ATP [30].

It was noted in previous studies that the composition of the Ce-Zr catalyst strongly affected the catalyst activity [31–34]. The optimum composition was found to depend on the nature of the pollutant to be decomposed, suggesting that it would always be necessary to tailor the catalyst composition for oxidizing a specific pollutant. Since wet oxidation is a radical reaction, the redox property of a catalyst is an important factor for controlling catalytic

* Corresponding author. Tel.: +1 302 831 2318; fax: +1 302 831 4545.
E-mail addresses: xiazhang@cczu.edu.cn (X. Li), cni@udel.edu (C. Ni).

activity [25]. To address the composition–activity relationship of a catalyst, many composition–dependent factors, especially structural and redox properties, should be taken into consideration. Over the past few years, CeO_2-containing materials have attracted intensive scrutiny for applications as catalysts [24,25,31–34]. When associated with transition metal oxides such as ZrO_2, CeO_2 demonstrates promoted oxygen storage and release capacity, enhanced oxygen mobility, and improved catalyst redox properties. Addition to CeO_2 of small amounts of ZrO_2 has been shown to affect remarkably the oxidation state of cerium [31,32].

Herein we report for the first time the preparation of ATP/$Ce_{1-x}Zr_xO_2$ nanocomposite via facile homogeneous precipitation. The synthetic parameters influencing the structure and morphology were investigated by various characterization techniques. The composite-activity effect on the catalytic wet oxidation of methylene blue was explored with finely tuned composition to understand the factors controlling the catalyst activity of this novel composite.

2. Experimentals

2.1. Materials and chemicals

Attapulgite powders were provided by Nanjing University Zijin Co. Ltd., Jiangsu, China. $Ce(NO_3)_3 \cdot 6H_2O$, $ZrOCl_2 \cdot 8H_2O$, hexamethylenetetramine, and methylene blue were purchased from China Chemical Reagent Co. Ltd. at analytical grade and used without further purification.

2.2. Synthesis of ATP/$Ce_{1-x}Zr_xO_2$ nanocomposites

Adequate amount of ATP was dispersed in 100 mL deionized water, followed by adding $Ce(NO_3)_3 \cdot 6H_2O$ and $ZrOCl_2 \cdot 8H_2O$ with magnetic stirring. Hexamethylenetetramine (molar ratio 1:5) was then added to the solution. The mixture was heated in a water bath of 80 °C for 2 h, and subsequently cooled in ambient environment to room temperature. The precipitate was washed with deionized water and absolute ethanol for three times. The resulting solid was dried in vacuum at 80 °C for 10 h, and subsequently calcined at 300 °C in air for 3 h. Specific parameters are shown in Table 1 below.

2.3. Materials characterization

TEM characterization was performed using a JEOL JEM-2100 transmission election microscope coupled with Gatan 832 CCD operating at an accelerating voltage of 200 kV. The samples were supported on carbon–copper grids by dropping ethanol suspensions containing uniformly dispersed oxide powder. FT-IR spectra were obtained using a Nicolet 460 with diffuse reflectance sampling accessory at a resolution of $4 \, cm^{-1}$, and the measurements were made using KBr powder as diluents. The powder X-ray diffraction (XRD) was performed with a Rigaku D/MAX-2500PC diffractometer

Table 1
Preparation parameters of ATP/$Ce_{1-x}Zr_xO_2$ samples.

Sample number	$Ce_{1-x}Zr_xO_2$ Loading (wt%)	x value
S1	10	0
S2	20	0
S3	30	0
S4	40	0
S5	50	0
S6	40	0.1
S7	40	0.2
S8	40	0.3
S9	40	0.4
S10	40	0.5

with Cu target (40KV, 40 mA). The average grain size d was estimated according to the Scherrer equation: $d = 0.89\lambda/\beta\cos\theta$, where θ is the diffraction angle of the main peak, β is the full width at half maximum (FWHM). Vis-Raman spectra were collected with a Renishaw (UK) spectrometer with an Ar ion laser of 514 nm excitation. The BET surface area was evaluated by N_2 sorption measurement using Micromeritics ASAP 2010 at 77 K. H_2-TPR was performed in a quartz reactor equipped with a Tianjin XQ TP5000 auto-adsorption apparatus using 50 mg catalyst. The samples were pretreated in N_2 (30 mL/min) at 423 K in order to drive away possible impurities. After cooling down to room temperature in N_2, the samples were heated at a rate of 10 K/min under the flow of a H_2 and N_2 mixture (5:95). The consumption of hydrogen was monitored by a built-in thermal conductivity detector. UV–vis spectra of dye solution after treatment for different time lengths were recorded using a UV-2550 Shimadzu UV–vis spectrophotometer.

2.4. Adsorption/catalytic activity measurements

The oxidation of methylene blue synthetic waste water was performed in a glass reactor with a capacity of 150 mL equipped with an O_3-flow controller. One gram of catalyst was introduced into 100 mL of synthetic wastewater and the initial concentration of methylene blue was 50 mg/L. The reaction was conducted at room temperature and atmospheric pressure, and the flow rate of O_3 was kept at 400 mL/min. The decomposition extent of the methylene blue was determined by measuring the value of the absorbance at 664 nm using a UV-722 spectrometer, and the decolorization rate D (%) was calculated according to the following formula:

$$D = \left(1 - \frac{A}{A_0}\right) \times 100\%$$

where A_0 is the initial absorbance of methylene blue solution and A is the final absorbance of methylene blue solution after treatment.

3. Results and discussion

3.1. Structural characterization

The morphology of the ATP/CeO_2 with various CeO_2 loadings is shown in Fig. 1a–e. The nanocomposite consists of 1-D fibrous structure with uniform diameters ranging from 40 to 50 nm and lengths ranging from 0.5 to 2 um. The CeO_2 nanoparticles with average diameter of 5 nm, together with small clusters of the CeO_2 nanoparticles, uniformly coat the surface of ATP when the weight percentage is relatively low (Fig. 1b). With gradual increase of CeO_2, the number of CeO_2 nanoparticles increases as well. The ATP are substantially wrapped by CeO_2 nanoparticles at 40 wt% (Fig. 1d), and few nanoparticles are observed to be detached from the surface of the nanorods. Fig. 1f shows an HRTEM image of sample S4, exhibiting well dispersed oxides surrounding an ATP fiber. Lattice fringes from CeO_2 {1 1 1}, {2 0 0}, {2 2 0} are clearly visible to have the interplanar spacing of 0.32, 0.27 and 0.19 nm respectively, consistent with the JCPDS (Joint Committee on Powder Diffraction Standards) data [35] and the calculation based on the corresponding spotty ring pattern in the same figure. In addition, the ring pattern confirms the face-centered cubic (fcc) structure of the crystalline CeO_2. Obvious aggregation of CeO_2 particles on the outside of the ATP rods appears when the CeO_2 content reaches 50% (Fig. 1e). The results also suggest that as the CeO_2 content increases, while the phase evolution does not significantly alter the general morphology of the ATP rods, adequate amount of CeO_2 can maintain a well-defined structure to achieve excellent immobilization of the nanoparticles. When loading amount is higher than 40 wt%, however, the abnormal precipitation and overgrowth of CeO_2 particles
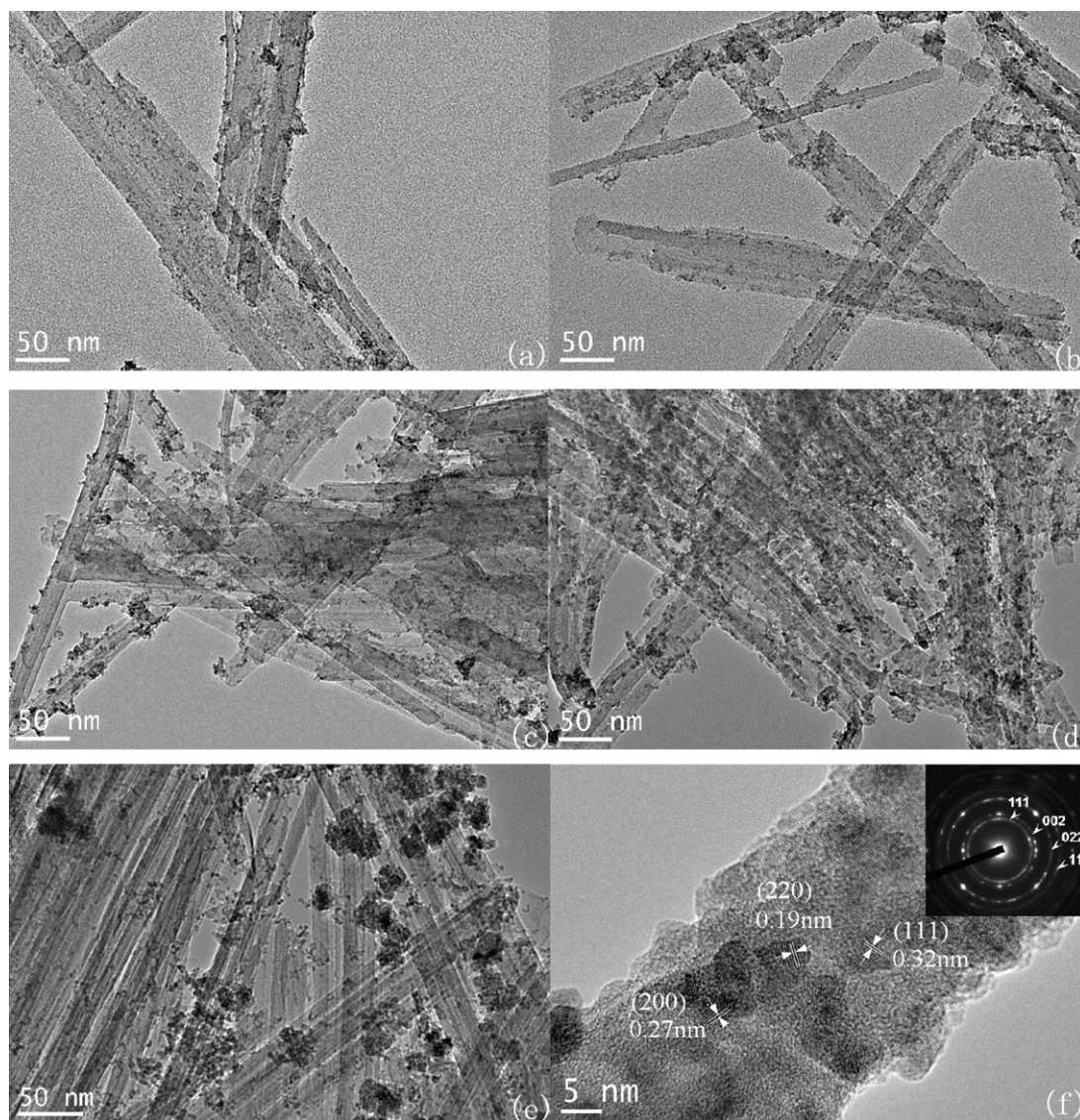
Fig. 1. TEM photographs of S1–S5 with various CeO_2 loadings (a) 10 wt%, (b) 20 wt%, (c) 30 wt%, (d) 40 wt%, (e) 50 wt%, and (f) HRTEM of a single rod in sample S4 and its selected area electron diffraction (SAED) pattern.

eventually lead to the appearance of obvious agglomeration of loaded oxide particles.

XRD patterns of S1–S5 and pure ATP are shown in Fig. 2. The diffraction peaks at the 2θ of 8.5°, 19.7° and 27.3° in Fig. 2 exhibit good agreement with the primary reflections from {1 1 0}, {0 4 0}, and {4 0 0} of the ATP [16,17]. Diffraction peak at 28.4° corresponds to {1 1 1} of the cubic fluorite structure of CeO_2, as identified using the standard JCPDS 34-0394 [31]. It is noticed that the {1 1 0} peak of ATP slightly shifts to higher Bragg angle with the increase of CeO_2, which can be attributed to the incorporation of O^{2-} from CeO_2 into the ATP support, resulting in the shrinkage of the basal distance of the ATP and at the same time, more O vacancies are left within CeO_2. Similar phenomena were observed by other researchers when CuO or TiO_2 was immobilized on ATP [19,20]. Another evidence of the introduction of ionic O^{2-} and probably also small amount of Ce^{4+} into the interlayers of the ATP is the decrease of ATP crystallinity as revealed by both XRD and SAED. It is worth noting that characteristic CeO_2 {1 1 1} peak shifts to higher Bragg angle as well. A plausible reason for decreased CeO_2 {1 1 1} spacing can be that cationic ions in ATP such as Mg^{2+}, Al^{3+} and Si^{4+} tend to diffuse into the CeO_2 lattice via interdiffusion, leading to the contraction of CeO_2 lattice because the radii of those ions are less than that of

Ce^{4+} ion. Such ionic interdiffusion also supports the observation of the immobilization of CeO_2 on the ATP support.

FT-IR was employed to further investigate the structure of the composite material (S4) as compared with raw ATP shown in Fig. 3. Two bonds at 3411 and 3551 cm^{-1} are assigned to the stretching vibration of zeolite water [13]. The bond at 1654 cm^{-1} is ascribed to the —OH bending mode of the adsorbed water molecules on surface. The bond at 1196 cm^{-1} corresponds to Si—O vibration mode in ATP [22]. The band at 792 cm^{-1} confirms the presence of quartz and the band at 475 cm^{-1} is also due to the bending vibration of Si—O—Si bonds [22]. Comparing the FT-IR spectra of ATP and S4, a new adsorption peak from S4 is revealed near 1384 cm^{-1}. It can be associated with the absorption peak of Ce—O bonds, implying the presence of rare earth oxides dispersed on the ATP surface in the form of CeO_2, which is consistent with the analysis of XRD patterns in Fig. 2.

According to an available CeO_2–ZrO_2 phase diagram, Zr^{4+} can substitute Ce^{4+} to form $Ce_{1-x}Zr_xO_2$ solid solutions over full range of the molar ratio [36]. However, $Ce_{1-x}Zr_xO_2$ can exist in three stable phases, monoclinic (m), tetragonal (t) and cubic (c), and two metastable phases (t', t'') under different conditions [31,32,37]. In addition to the above single phase regions, two adjacent phases in
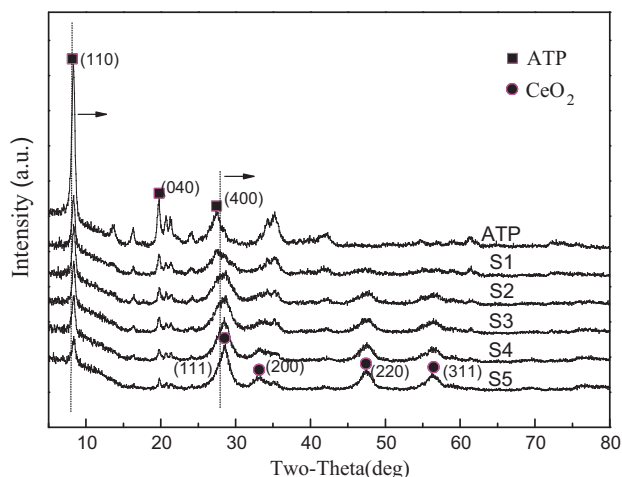
Fig. 2. XRD patterns of natural ATP and ATP/CeO$_2$ samples with various CeO$_2$ loadings.
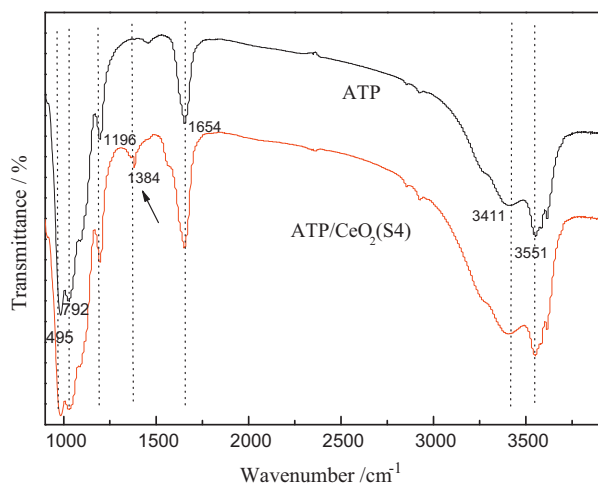

Fig. 3. FT-IR spectra of ATP and ATP/CeO$_2$ (S4).

the phase diagram can coexist in some composition ranges as the Gibbs' phase rule dictates. In this study, XRD and electron diffraction indicate that the oxide have homogeneous face-centered cubic structure with the absence of zirconium oxide phase for various atomic fractions as can be seen in Figs. 4 and 5, where the latter
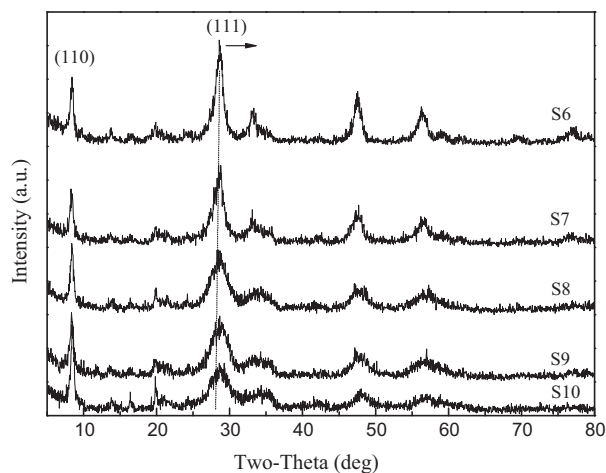

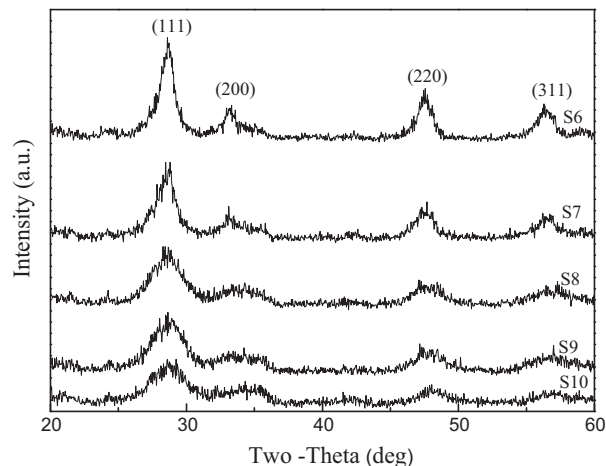**Fig. 4.** XRD patterns of ATP/Ce$_{1-x}$Zr$_x$O$_2$ composites with various Zr^{4+} dopants.

Fig. 5. XRD patterns of Ce$_{1-x}$Zr$_x$O$_2$ oxides on ATP surface in a narrow range.

shows the XRD patterns of Ce$_{1-x}$Zr$_x$O$_2$ oxides on ATP surface from 20° to 60°. No evidence of the presence of other phases (m, t, t', t'', or ZrO$_2$) was detected. A consistent peak broadening is observed, reflecting the occurrence of more defective ceria lattice, lower degree of crystallinity, and smaller particle size. With increasing zirconium content, a progressive shift of the diffraction peaks to higher Bragg angles is also observed. This shift indicates that part of zirconium species enters into the ceria lattice and aggravates the contraction of its unit cell, which may be due to the substitution of Ce^{4+} (97 pm) by relatively smaller ionic radius Zr^{4+} (84 pm), consequently leading to lattice distortion as well as the formation of more oxygen vacancies [34], both of which enhance the catalytic oxidation capability of the composites.

Since there are two competing effects on the peak-shift in XRD with various doping concentrations of ZrO$_2$, including contraction by the replacement of Ce^{4+} by Zr^{4+} and expansion by the increased fraction of Ce^{3+} or more oxygen vacancies, vis-Raman is necessary for the determination of crystal phases. Fig. 6 exhibits the Raman spectra of ATP/Ce$_{1-x}$Zr$_x$O$_2$ nanocomposites from 100 to 800 cm^{-1}. High-intensity phonon vibration appears around 465 cm^{-1} in all samples and is attributed to the symmetric F_{2g} mode for cubic CeO$_2$ [31]. There is no evidence of the presence of t-ZrO$_2$ as it would associate with six Raman-active modes ($A_{1g} + 2B_{1g} + 3E_g$) of symmetry centered around 147, 268, 313, 460, 600 and 645 cm^{-1} according to the literature [32], manifesting a homogeneous distribution of Ce and Zr in the single phase Ce$_{1-x}$Zr$_x$O$_2$. In other words, the
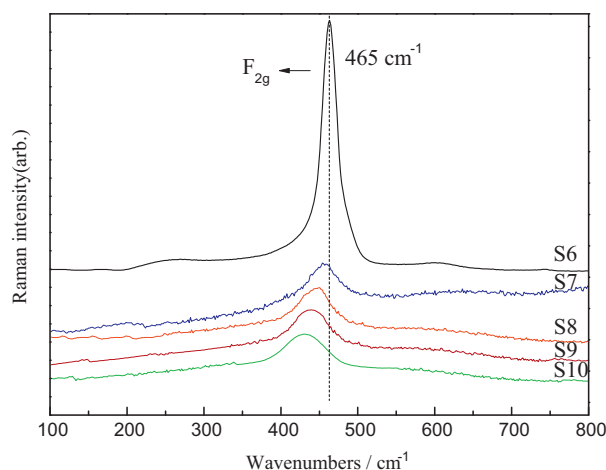

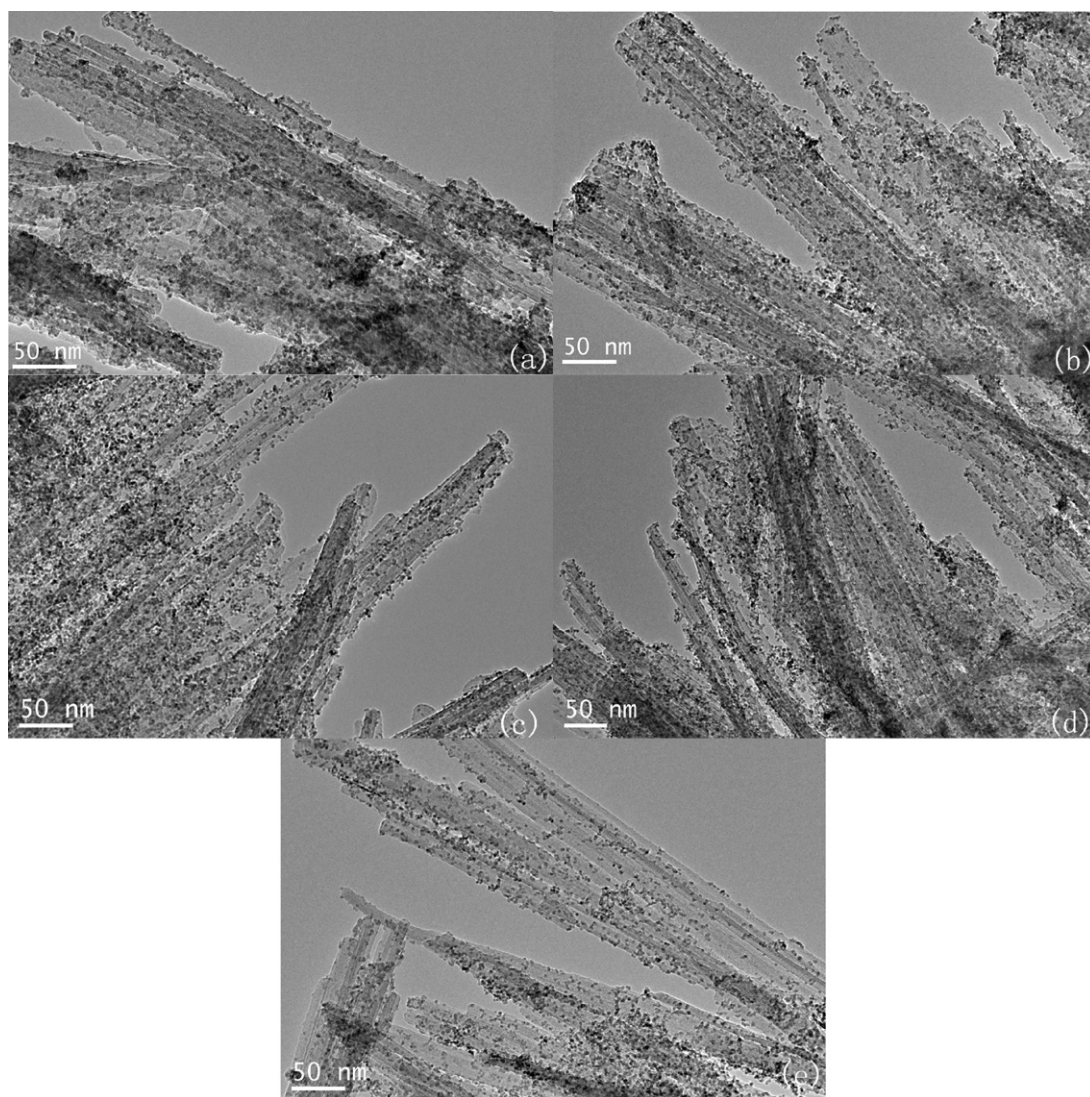**Fig. 6.** Raman spectra of S6–S10 with various Zr^{4+} dopants.

Fig. 7. TEM photographs of S6–S10 with various Zr^{4+} dopants (a) $x = 0.1$, (b) $x = 0.2$, (c) $x = 0.3$, (d) $x = 0.4$, (e) $x = 0.5$.

$Ce_{1-x}Zr_xO_2$ preserves the fcc structure and exists as a solid solution, consistent with the aforementioned XRD results. It is noticed that the intensity of F_{2g} decreases with the increase of x value, along with a progressive peak shift of the spectra towards the lower wavenumber, revealing structural distortion due to oxygen vacancies and metal doping of smaller ionic radius.

3.2. Textural characterization

The TEM micrographs of $ATP/Ce_{1-x}Zr_xO_2$ nanocomposites with various Zr^{4+} dopants shown in Fig. 7 indicate that the nanoparticles and their small clusters are evenly dispersed on the ATP surface and the Zr^{4+} doping does not significantly alter the morphology of the composites as compared with Fig. 1d. Textural properties of $ATP/Ce_{1-x}Zr_xO_2$ nanocomposites with various Zr^{4+} dopants are summarized in Table 2. The particle sizes calculated by XRD and TEM slightly decrease with the increasing x value. The BET surface area has an increase from $133.6 \, m^2 \, g^{-1}$ to $161.8 \, m^2 \, g^{-1}$ when x value changes from 0 to 0.1, which may be associated with large lattice distortion [25] and increased surface defectivity resulting from the Zr^{4+} dopant introduction, and the increased surface area potentially contributes to the enhancement of catalytic reactivity. However, there is no additional obvious difference observed in the BET surface area measurement as the x value further increases to

0.5. Generally, the textural properties including particle size and surface area are of importance to the catalytic performance of catalysts. The reflection of the nanoparticle size effect is considered to be negligible since the quantitative variation is in a very close range. The reducibility of the nanocomposites is expected to ascertain the influence of structural effects.

3.3. Redox properties

The H_2-TPR profiles for $ATP/Ce_{1-x}Zr_xO_2$ nanocomposites are presented in Fig. 8. With increasing Zr content, the peaks have an obvious trend shifting to lower temperatures, for instance, from

Table 2
Textural properties of $ATP/Ce_{1-x}Zr_xO_2$ nanocomposites.

Molar fraction x	$d_{(XRD)}$/nm[a]	$d_{(TEM)}$ nm[*]	BET surface area ($m^2 \, g^{-1}$)
$x = 0$	5.3	4.9–5.4	133.6
$x = 0.1$	5.0	4.8–5.2	161.8
$x = 0.2$	4.9	4.6–5.0	167.5
$x = 0.3$	4.8	4.4–4.9	165.4
$x = 0.4$	4.6	4.3–4.9	162.3
$x = 0.5$	4.5	4.1–4.7	169.0

[a] $d_{(XRD)}$ and $d_{(TEM)}$ represent the particle size of Ce—Zr—O oxides on ATP surface calculated by Scherrer equation and TEM, respectively.

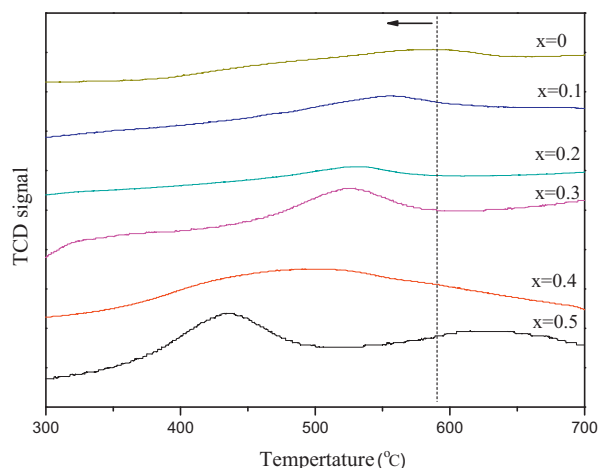**Fig. 8.** H$_2$-TPR profiles for ATP/Ce$_{1-x}$Zr$_x$O$_2$ nanocomposites with various Zr^{4+} dopants. Consecutively from top to bottom, $x = 0$, $x = 0.1$, $x = 0.2$, $x = 0.3$, $x = 0.4$, $x = 0.5$.

Fig. 10. UV–vis spectra of methylene blue after different treating time with sample S7 and bubbling O$_3$.

592 °C for $x = 0$ to 439 °C for $x = 0.5$, along with a gradual increase of peak intensity, revealing increased oxygen mobility and vacancies caused by Zr^{4+} incorporation. In agreement with the XRD results shown in Fig. 4, the doping effect of Zr^{4+} contributes to decreasing lattice constant, reducing activation energy for oxygen diffusion within the lattice, and consequently favoring for the reduction [32]. The structural defects promoted by the introduction of Zr^{4+} are also expected to play an important role in redox behavior as well as catalytic activity.

3.4. Catalytic oxidation properties

Utilizing the ATP/Ce$_{1-x}$Zr$_x$O$_2$ nanocomposite, the degradation of methylene blue was investigated. The decolorization efficiency is shown in Fig. 9 as a function of treating time. Without using any catalysts, the decolorization efficiency by O$_3$ bubbling is 42% in 240 min, which indicates that the oxidation ability of O$_3$ is very limited. Adding ATP, the decolorization efficiency increases to 73% after reaction for 240 min due to the adsorption capability of ATP. With ATP/CeO$_2$ composite, the decolorization efficiency rises slightly to 82% and the small efficiency increment is attributable to the catalytic oxidation offered by CeO$_2$. When ATP/Ce$_{1-x}$Zr$_x$O$_2$ is used, on the other hand, the decolorization efficiency reaches as high as 99% for S7 during the same period of time, which indicates that doping CeO$_2$ with Zr^{4+} plays a considerable role in the enhancement of
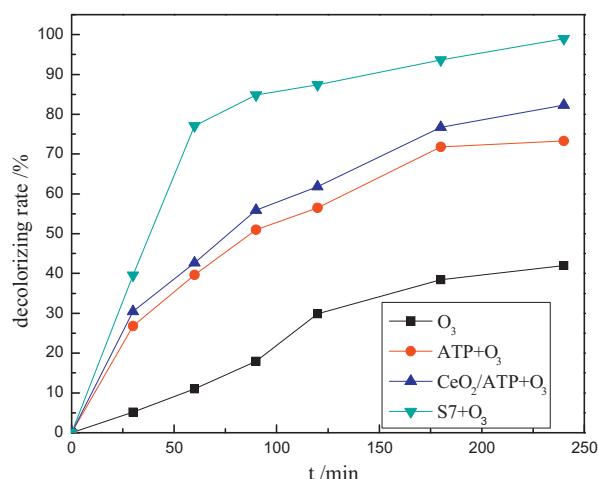
catalytic activity. The ATP/Ce$_{1-x}$Zr$_x$O$_2$ nanocomposite interacts with O$_3$ to generate more radicals to attack dye molecules. Previous studies demonstrated that the main function of wet oxidation catalyst was to directly or indirectly interact with the substrate to produce active radicals in the first step of the reaction [24,25]. Herein the direct interaction of the active sites (Ce^{4+}) and the substrate (RH) can be represented by a simplified mechanism in which the OH$^\bullet$ is proposed to be generated by a free radical chain auto-oxidation process as follows:

$$RH + Ce^{4+} \rightarrow R^\bullet + H^+ + Ce^{3+} \quad \text{(initiation)} \tag{1}$$

$$R^\bullet + O_3 \rightarrow RO_2^\bullet + O_2 \quad \text{(propagation)} \tag{2}$$

$$RO_2^\bullet + RH \rightarrow ROOH + R^\bullet \quad \text{(propagation)} \tag{3}$$

$$ROOH \rightarrow RO^\bullet + OH^\bullet \quad \text{(autocatalyticdegradation)} \tag{4}$$
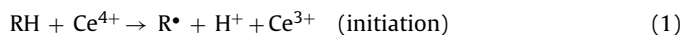
Reaction (1) occurs on the surface of ATP/Ce$_{1-x}$Zr$_x$O$_2$ nanocomposite, which is a fast step. Reactions (2) and (3) play crucial role in the generation of OH$^\bullet$ radicals during the propagation step. Therefore, increasing the active sites and O$_3$ amount can facilitate reactions to produce OH$^\bullet$, consequently, promoting the degradation efficiency of organic pollutants in the final step of reaction (4).

The UV–vis spectra of methylene blue in Fig. 10 indicates that there are two major absorbance peaks, 614 nm and 664 nm, which are attributable to the monomer and dimer of methylene blue [24]. These two absorbance peaks become weaker gradually in intensity as the treating time increases, and after treatment for 240 min, the two peaks almost disappear completely, indicating the majority of the monomer and dimer in methylene blue is destroyed.

The performance of the Ce$_{1-x}$Zr$_x$O$_2$/ATP catalyst can be correlated to the redox potential of Ce^{4+}/Ce^{3+} couple, a distinctive and essential property of Ce$_{1-x}$Zr$_x$O$_2$. For the activation of O$_3$ subsequent to its adsorption, O$_2^{2-}$ (peroxide) likely stabilized by Ce^{4+} has been detected on ceria [25]. In the oxidation of hydrocarbons, an electron-rich surface of a catalyst, such as ATP/Ce$_{1-x}$Zr$_x$O$_2$, has the ability to activate O$_3$ to O$_2^{2-}$. The numerous oxidation sites of the novel ATP/Ce$_{1-x}$Zr$_x$O$_2$ then facilitate electron transfer processes in the radical producing step of the wet oxidation. The Zr^{4+} substitution further promotes the formation of the oxidation sites according to the H$_2$-TPR results. However, it is evident as shown in Fig. 11 that the doping effect is not monotonic. The decolorization efficiency increases when the x value is lower than 0.2 but decreases when x value is higher than 0.2. A possible reason is that additional substitution of Zr^{4+} beyond x value 0.2 results in insufficient

Fig. 9. Comparison of catalytic oxidation of methylene blue by various composites.
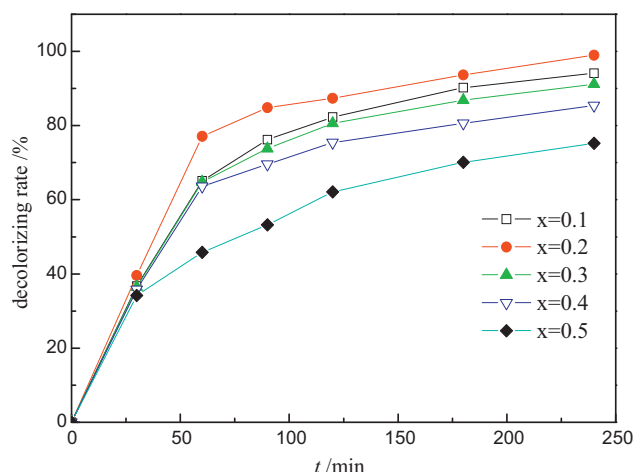
Fig. 11. Molar fraction of Zr^{4+} dopant vs decolorization efficiency of methylene blue.

initiation, the step (1) in the free radical chain auto-oxidation process, despite the fact that increased structural defects are favorable for the generation of radical $OH^\bullet$. This suggests that to achieve best catalytic and redox performances, optimal doping with an x value $\sim$0.2 is necessary to maximize the synergistic effect between the catalyst and the oxidant.

4. Conclusions

In summary, we have developed a facile synthetic route for the preparation of novel $ATP/Ce_{1-x}Zr_xO_2$ nanocomposite. The oxide nanoparticles of about 5 nm are successfully immobilized with uniform dispersion on the surface of attapulgite fibers when the loading is up to 40 wt%. Catalytic oxidation removal of methylene blue has been evaluated for the nanocomposite with various compositions. It is found that the catalytic oxidation property of the $ATP/Ce_{1-x}Zr_xO_2$ is superior to both single component attapulgite and ATP/CeO_2. The molar fraction x in $ATP/Ce_{1-x}Zr_xO_2$ has significant impact on the degradation efficiency. The best $ATP/Ce_{1-x}Zr_xO_2$ catalyst is obtained when $x=0.2$ at which a 99% decomposition of methylene blue in 240 min is achieved.

Acknowledgments

References

[1] Z.W. Xu, W.M. Zhang, L. Lv, B.C. Pan, P. Lan, Q.X. Zhang, Environ. Sci. Technol. 44 (2010) 3130–3135.
[2] I.P. Chen, S.S. Lin, C.H. Wang, S.H. Chang, Chemosphere 66 (2007) 172–178.
[3] P.G. Hoertz, Z. Chen, C.A. Kent, T.J. Meyer, Inorg. Chem. 49 (2010) 8179–8181.
[4] I. Ogino, B.C. Gates, J. Am. Chem. Soc. 130 (2008) 13338–13346.
[5] F. Li, B.C. Gates, J. Phys. Chem. C 111 (2007) 262–267.
[6] P.J. Smeets, J.S. Woertnk, B.F. Sels, E.I. Solomon, R.A. Schoonheydt, Inorg. Chem. 49 (2010) 35573–43583.
[7] A. Uzum, B.C. Gates, J. Am. Chem. Soc. 131 (2009) 15887–15894.
[8] H. Zhang, Z. Li, P. Xu, R. Wu, Z. Jiao, Chem. Commun. 46 (2010) 6783–6785.
[9] S. Das, T. Asefa, ACS Catal. 1 (2011) 502–510.
[10] Y. Fang, D. Gu, Y. Zou, Z.X. Wu, F.Y. Li, R.C. Che, Y.H. Deng, B. Tu, D.Y. Zhao, Angew. Chem. Int. Ed. 49 (2010) 7987–7991.
[11] S.J. Guo, S.J. Dong, E. Wang, ACS Nano 4 (2010) 547–555.
[12] D.P. He, C. Zeng, C. Xu, N.C. Cheng, H.G. Li, S.C. Mu, M. Pan, Langmuir 27 (2011) 5582–5588.
[13] L. Bouna, B. Rhouta, M. Amjoud, F. Maury, M.C. Lafont, A. Jada, F. Senocq, L. Daoudi, Appl. Clay Sci. 52 (2011) 301–311.
[14] P. Aranda, R. Kun, M.A. Martin-Luengo, S. Letaief, I. Dekany, E. Ruiz-Hitzky, Chem. Mater. 20 (2008) 84–91.
[15] Y.X. Jia, W. Han, G.X. Xiong, W.S. Yang, J. Colloid Interface Sci. 323 (2008) 326–331.
[16] C.L. Christ, Am. Mineral. 54 (1969) 198–205.
[17] M.S. Barrios, V.F. Gonzalezl, A.V. Rodriguezm, Apply. Clay Sci. 10 (1995) 247–251.
[18] Y.S. Liu, P. Liu, Z.X. Su, F.S. Li, F.S. Wen, Appl. Surf. Sci. 255 (2008) 2020–2025.
[19] J.L. Cao, G.S. Shao, Y. Wang, Y.P. Liu, Z.Y. Yuan, Catal. Commun. 9 (2008) 2555–2559.
[20] D.F. Zhao, J. Zhou, N. Liu, Mater. Sci. Eng. A 431 (2006) 256–262.
[21] D.F. Zhao, J. Zhou, N. Liu, Mater. Charact. 58 (2007) 249–255.
[22] C.L. Huo, H.M. Yang, Appl. Clay Sci. 50 (2010) 362–366.
[23] L.L. Zhang, F.J. Lv, W.G. Zhang, R.Q. Li, H. Zhong, Y.J. Zhao, Y. Zhang, X.J. Wang, Hazard. Mater. 171 (2009) 294–300.
[24] Y. Liu, D. Sun, Appl. Catal. B 72 (2007) 205–211.
[25] H.Y. Chen, A. Sayari, A. Adnot, F. Larachi, Appl. Catal. B 32 (2001) 195–204.
[26] Z.K. Zhao, M.M. Yung, U.S. Ozkan, Catal. Commun. 9 (2008) 1465–1471.
[27] C.Y. Shiau, M.W. Ma, C.S. Chuang, Appl. Catal. A 301 (2006) 89–95.
[28] M. Triki, Z. Ksibi, A. Ghorbel, F. Medina, Microporous Mesoporous Mater. 117 (2009) 431–435.
[29] J. Wang, Y. Lv, L. Zhang, B. Liu, R. Jiang, G. Han, R. Xu, X. Zhang, Ultrason. Sonochem. 17 (2010) 642–648.
[30] Z.G. Chen, F. Chen, X.Z. Li, X.W. Lu, C.Y. Ni, X.B. Zhao, J. Rare Earths 28 (2010) 566–570.
[31] X.Z. Li, C.Y. Ni, F. Chen, X.W. Lu, Z.G. Chen, J. Solid State Chem. 182 (2009) 2185–2190.
[32] M.L. Teng, L.T. Luo, X.M. Yang, Microporous Mesoporous Mater. 119 (2009) 158–164.
[33] Z.Q. Wang, Y.M. Zhou, Y.Q. Sun, K. Fan, X.X. Guo, X.L. Jiang, J. Solid State Chem. 182 (2009) 2130–2134.
[34] W.T. Chen, K.B. Chen, M.F. Wang, S.F. Weng, C.S. Lee, M.C. Lin, Chem. Commun. 46 (2010) 3286–3288.
[35] Z.L. Wang, X.D. Feng, J. Phys. Chem. B 107 (2003) 13563–13566.
[36] M. Yashima, K. Morimoto, N. Ishizawa, M. Yoshimura, J. Am. Ceram. Soc. 76 (1993) 1745–1750.
[37] X. Liang, X. Wang, Y. Zhuang, B. Xu, S. Kuang, Y.D. Li, J. Am. Chem. Soc. 130 (2008) 2736–2737.